The use of x-ray tomography to investigate soil deformation around growing roots

A. Floriana, E. Andò, G. Viggiani, N. Lenoir, R. Peyroux, Chloé Arson, Luc Sibille

Anselmucci, F. *et al*. (2021) ***Géotechnique Letters*** **11**, 1–7, https://doi.org/10.1680/jgele.20.00114

Use of x-ray tomography to investigate soil deformation around growing roots

F. ANSELMUCCI*, E. ANDÒ†, G. VIGGIANI‡, N. LENOIR§, R. PEYROUX‖, C. ARSON** and L. SIBILLE††

The increased shear strength of rooted soil recently inspired researchers to assess the stability of vegetated slopes with continuum models and to design anchors by mimicking root system architectures. Yet, there is no clear understanding to date of why roots affect soil properties. This paper presents an experimental proof of concept based on x-ray tomography that addresses this issue by assessing soil microstructural changes induced by root growth. A three-dimensional time series of the root–soil interaction was imaged for 7 days. The computed local strain tensor highlights that the soil was sheared in the vicinity of the root system. Additionally, the initial bulk density of the soil was found to significantly influence the response of soil to plant root growth. In the sheared zone, the looser soil exhibited a slightly contractant behaviour, while the denser soil was purely dilatant. Further from the root system, no significant volume changes were measured for the denser specimen, whereas compaction was noted in the looser specimen. In contrast with earlier studies, results suggest that the high soil porosity near the root may result not only from steric exclusion, but also from the constitutive soil response to shear deformation.

KEYWORDS: laboratory tests; strain; vegetation

BACKGROUND

It is well known that soils that contain roots have a higher shear strength than soils that do not (Świtala *et al*., 2018). With the emergence of bio-inspiration in geotechnics, researchers have recently explored the use of additive manufacturing for designing anchoring systems (Mallett *et al*., 2018). Recognising that the root system architecture (RSA) is a signature of plant development, other groups studied the adaptation of root topology to obstacles (Jin *et al*., 2020) and assessed the feasibility of using plant-inspired network dynamics algorithms to optimise infrastructure (Patino-Ramirez & Arson, 2020). The Cam-Clay model extended to unsaturated soils (Tamagnini, 2004) was modified to account for root strength and evapotranspiration in order to simulate vegetated slopes (Świtala *et al*., 2019, Świtala, 2020). Yet, much is still unknown on the microscopic processes that control soil/root mechanical interactions, and on how these micromechanisms yield a higher bulk shear strength. A better understanding of soil microstructural changes on root growth would enhance the prediction capabilities of continuum-based models and offer more avenues for bio-inspired geotechnical design (e.g. Martinez *et al*., 2021). This study, therefore, aims to quantify the mechanical effects of plant root growth on soil microstructure evolution.

The mechanical interactions of a growing root with the surrounding soil are complex.

There are many factors at play: the mechanical properties of the soil and its initial state (density, pore-size distribution, stress, water content), the root itself, hairs and exudates of the root (Carminati & Vetterlein, 2013; Koebernick *et al*., 2017), the loss of the pore water due to evapotranspiration, the ratio of root diameter to typical pore size and the connectivity of the soil macroporosity (Lucas *et al*., 2019). To penetrate a soil, an individual root must either displace soil material by a combination of rigid-body movement, shear and compression (Bengough *et al*., 2011) or follow the path of an existing pore network (White & Kirkegaard, 2010) (if the root can fit inside the pores). All of these actions modify the microstructure of the surrounding soil, and thus alter its mechanical and physical properties.

Most of the previous studies focused on the effect that roots have on the soil physical properties up to a few millimetres from the root. As roots mature, their growth and their exudates alter the soil water potential (Hinsinger *et al*., 2009). Rhizosphere properties evolve in time, depending on the root age (Carminati & Vetterlein, 2013). For instance, root hairs improve root–soil contact and increase the soil aggregation (Moreno-Espíndola *et al*., 2007). The impact of roots on soil porosity in the rhizosphere has been extensively investigated. An increase of the macro-porosity of the soil in direct contact with the root is often observed (Helliwell *et al*., 2019). Helliwell *et al*. (2017) explained such an increase of porosity by the geometrical constraint brought by the root: grains pack more loosely near a flat object (root) than against other grains. Further in the rhizosphere, the change of porosity may be either positive or negative (Tracy *et al*.,

Manuscript received 20 August 2020; first decision 5 February 2021; accepted 5 February 2021.
*University of Grenoble Alpes, CNRS, Grenoble INP, Grenoble, France (Orcid:0000-0002-2180-7546).
†University of Grenoble Alpes, CNRS, Grenoble INP, Grenoble, France (Orcid:0000-0001-5509-5287).
‡University of Grenoble Alpes, CNRS, Grenoble INP, Grenoble, France (Orcid:0000-0002-2609-6077).
§University of Grenoble Alpes, CNRS, Grenoble INP, Grenoble, France (Orcid:0000-0003-3517-0627).
‖University of Grenoble Alpes, CNRS, Grenoble INP, Grenoble, France (Orcid:0000-0002-6199-4817).
**School of Civil and Environmental Engineering, Georgia Institute of Technology, Atlanta, GA, USA (Orcid:0000-0002-4477-1072).
††University of Grenoble Alpes, CNRS, Grenoble INP, Grenoble, France (Orcid:0000-0002-3510-3400).

2012). Nevertheless such modifications of the porosity of the soils, and how it evolves with the distance from the root, depend on the initial soil density, the connectivity of the macropores (Helliwell *et al*., 2019; Lucas *et al*., 2019) and the root density (Bodner *et al*., 2014). Besides, in some cases, investigation tools may affect the results. Mooney *et al*. (2012) reviewed the application of x-ray computed tomography (XRCT) in root visualisation studies in the last 40 years, and concluded that XRCT has a good potential to unravel the complex interaction between roots and soil. Finally, Keyes *et al*. (2016, 2017) used *in vivo* XRCT combined with digital image correlation (DIC) to map soil deformation, quantifying only the soil kinematics around a growing root tip at different time steps within 1 h of observation.

In this study, the authors measure displacements and determine strain fields to assess the microstructural changes induced by a maize root growing in sand, not only in the vicinity of the root, but also up to few centimetres far from the root. Within the first few days of plant growth, *in vivo* four-dimensional XRCT and three-dimensional (3D) DIC were used to observe and measure the kinematics of the root–sand system with time. Furthermore, the novelty of this study is to extend the analysis far from the root and for 7 days.

GRANULAR MATERIAL PREPARATION

The soil used was Hostun HN31 sand, a fine-grained, angular siliceous sand coming from the Hostun quarry (Drôme, France). Table 1 summarises its index properties (Canou, 1989; Flavigny *et al*., 1990).

The sand was dry pluviated into a cylindrical poly(methyl methacrylate) (PMMA) tube, the diameter of which was chosen to optimise the trade-off between pixel size and field of view during x-ray imaging (which encourages small diameters for small pixel sizes), as well to avoid strong boundary effects during pluviation and root growth (which encourages larger diameters). After a series of trials, a diameter of 50 mm and a height of 100 mm were selected in order to have a pixel size of 40 μm. Pluviation was performed with drop heights of 2 and 100 mm, which yielded relative densities D_R of 30 and 80%, respectively.

Table 2 summarises the pluviation parameters used.

SEED PREPARATION

Among all the crops that generate fibrous RSAs, a wild-type of maize (*Zea mays* L.) was used for this study. A fibrous root system was chosen over other root types because it consists of groups of roots of similar sizes. These create a thick network which secures efficient uptake of water and nutrients while providing anchorage (Lynch, 1995). Seeds were sterilised in a solution of 15% bleach in distilled water for 15 min and then rinsed in distilled water. Thereafter, seeds were transferred in culture dishes between wet filter papers, foil-wrapped and germinated for 48–60 h at a fixed temperature of 19 ± 2°C. Seeds with a germinated root, called radicle, of about 10–15 mm long were selected.

Table 1. Hostun sand index properties: mean grain size $\sim D_{50}$, coefficient of uniformity $C_u = D_{60}/D_{10}$, coefficient of gradation $C_g = (D_{30})^2/(D_{60}D_{10})$, minimum and maximum void ratio and specific gravity G_s

	D_{50}: mm	C_u	C_g	e_{min}	e_{max}	G_s
HN31	0·338	1·5	1	0·648	1·041	2·65

Source: Canou (1989), Flavigny *et al*. (1990).

Table 2. Summary of pluviation parameters

Pluviation parameters	Looser, $D_R = 30\%$	Denser, $D_R = 80\%$
Drop height: mm	2	100
Funnel opening width: mm	7	7
Pouring rate: cm^3/s	1·51–1·64	2·45–2·80

GRANULAR SAMPLE PREPARATION WITH SEED

The germinated seed was radially centred in the cylindrical tube during sand pluviation at a depth of 1·5–2 times the seed height. The radicle was always pointing downward. A base was specifically designed with a pattern of holes which enabled sample watering from the bottom. Unlike field soil, sand cannot provide any nutrients for the root system. The water was consequently enriched with soluble plant feed (detailed in Table 3) before being introduced in the system. Watering was done at day 0 and then interrupted during the 7 day period of tomography.

OBSERVATION TOOLS AND IMAGE PROCESSING

3D images were acquired using the x-ray scanner at Laboratoire 3SR, specifically designed by RX-Solutions (Annecy, France). For each initial density, three samples were observed and the one with the most promising root growth was scanned throughout a week. Each sample was scanned at 135 kV source voltage with a 0·2 mm copper filter; two vertically stacked scans of 1120 projections (each 1536 × 1920) were acquired at a pixel size of 40 μm; the entire process took just under 2 h. The acquired radiographs were reconstructed into a 3D volume using the software X-Act provided by the system manufacturer.

The first tomography was performed the day when the seedling was placed in the sand sample. Thereafter, each sample was scanned at 24 h intervals. In this study the evolution of the seed–sand sample was scanned eight times, which was sufficient to obtain a root system with embryonic roots such as primary and seminal roots, as well as post-embryonis, laterals and crown roots (Hochholdinger, 2009) for both sand densities studied. Figure 1 summarises the steps followed to obtain the 3D reconstruction of the specimens.

A specifically designed image segmentation technique based on variance and bilateral filtering as well as thresholding was used to identify the root growth into the sand sample (Anselmucci *et al*., 2019). Figure 2 shows root systems extracted from the tomographies for denser and looser sand states. The mean root diameter φ_R, in both cases, is 0·57 ± 0·1 mm, however, the effect of the sand density on

Table 3. Details of the chemical components within the soluble plant feed – Vitafeed 111 (Vitax company)

Chemical components	Mass percentage
Total nitrogen (N)	19%
Phosphorus pentoxide (P_2O_5) soluble in neutral ammonium citrate and in water	19% (8·3%P)
Phosphorus pentoxide (P_2O_5) soluble in water	19% (8·3%P)
Potassium oxide	19% (15·8%K)
Borin (B) soluble in water	0·15%
Total copper (Cu)	0·025%
Total iron (Fe)	0·05%
Total zinc (Zn)	0·009%
Total manganese (Mn)	0·025%

the development of the root system is clearly visible. The elements composing the root system are concentrated in the upper part of the denser sand sample whereas the whole height of looser sand sample is investigated by the root system.

Digital volume correlation (DVC) was used to measure rearrangements between two imaged states.

Given two-textured 3D volumes with small rearrangements, DVC entails the optimised search for a transformation function that best matches the volumes. In this study a *local* approach was used, whereby the reference (initial) 3D image was split into regular cubes whose dimension was set such that there is sufficient texture to be able to match changes, and independent linear transformation functions were solved for each cube.

The reconstructed images were binned by averaging the grey values of $2 \times 2 \times 2$ together, the pixel size was consequently doubled to 80 μm – this operation divides data volume by a factor 8 and also denoises significantly, at the (possible) cost of spatial resolution. The regular grid was composed of $40 \times 40 \times 99$ non-overlapping cubic correlation windows measuring $17 \times 17 \times 17$ voxels – that is, $1{\cdot}36 \times 1{\cdot}36 \times 1{\cdot}36$ mm^3. The local DVC code, in the free and open-source software spam (Andò *et al.*, 2017; Stamati *et al.*, 2020) was used in this study.

KINEMATICS

Figure 3 presents 3D vectorial *displacement* fields where the displacement vector is extracted from the measured linear transformation function for each correlation window. Each displacement vector is the displacement from day 0 until the day shown, and each displacement vector is shown in the centre of its cube. Arrows are scaled by 10 and are also coloured according to a colour map, which is also proportional to the length of the displacement vector. The identified root system is plotted in the same coordinate system in green.

For both densities, measured displacements are clearly situated around the roots, and the most significant displacements occur in the areas with higher root density.

The fields in Fig. 3 suggest that displacements are induced by the growth of the root system. The maximum displacement magnitude is about 0·95 mm (i.e. $[2{\cdot}9]D_{50}$) and 1·6 mm (i.e. $[3{\cdot}5]D_{50}$) for the looser and the denser states, respectively. In the looser specimen, the main root keeps growing after reaching the bottom of the container (after day 4), producing displacements about twice the mean grain size.

STRAINS

Using the displacement field, local strain invariants were computed in the finite strain framework using a 3D implementation of the method proposed by Geers *et al.* (1996) (using a spherical structuring element of radius two as implemented in spam-regularStrain). The first invariant – the volumetric strain – is noted ε_v and is obtained from the determinant of the transformation gradient (**F**)−1. The second invariant – Euclidean norm of the deviatoric part of the strain tensor – representing the intensity of the shear deformation is noted ε_q.

Horizontal projections of the total (i.e. computed from day 0) deviatoric and volumetric strain fields are presented in Fig. 4. The deviatoric strain plotted is a 'maximum' projection, whereby the maximum value of deviatoric strain in the plane of observation is kept. In contrast, the volumetric strain plotted is the mean of the field in the axis of observation.

The deviatoric strain field shows that root produces shear strain around itself (Fig. 4). Shear deformations are predominant around the root; they are initiated by the elongation of the root tip, but do not present significant evolution once the tip has passed. Similar behaviour was found by Keyes *et al.* (2016), in a study of the effect of maize roots on soil.

Moving now to the volumetric strain field, dilation ($\varepsilon_v < 0$) is also predominant in the vicinity of the roots which is partially in agreement with some previous results concerning the porosity changes in the rhizosphere (Bodner *et al.*, 2014;

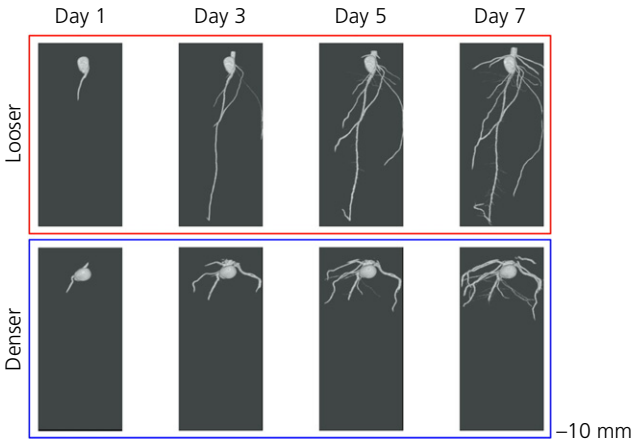

Fig. 2. 3D maize root systems evolution on selected days for looser and denser sand specimens

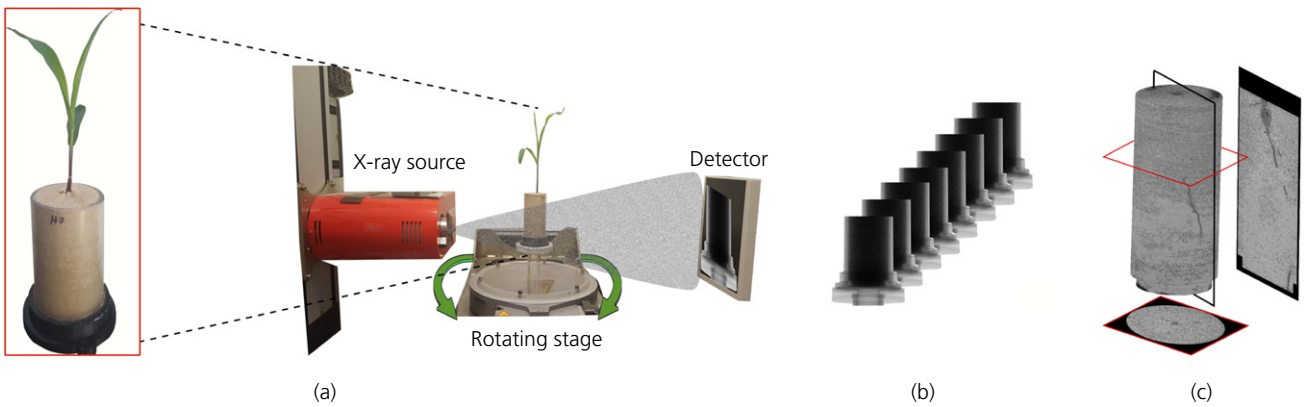

Fig. 1. Steps for sample tomography; (a) x-ray set-up, (b) 2D radiographs, (c) 3D reconstruction

Lucas *et al.*, 2019). Further from the root system, no significant volume changes are measured for the denser specimen, whereas in the looser specimen the soil tends to compact. This behaviour is confirmed in a backup experiment on a similar loose sample. The first 3 days of observation reveal that in the denser sample, dilation occurs radially up to 10–12D_{50} from the root surface in the plane perpendicular to the root axis, while it propagates up to 14D_{50} below the tip, but with a lower intensity. In the looser sample, the soil dilates up to a distance of 7·6–8D_{50} from the root surface both radially and below the tip. The two-dimensional (2D) profile of a 'sheared' volume around the root system is defined as the region with $\varepsilon_q > 1\%$. Figure 5 shows the contour of this zone with a dotted green line, superimposed on the volumetric strain field. The thickness of the sheared zone depends on the sand initial density: wider in the looser case ($\sim 10\varphi_R$) than in the denser one ($\sim 8\varphi_R$). The coupling between ε_v and ε_q depends strongly on the initial density (as expected): in the looser sample both dilation and contraction are observed in the sheared zone, while slight contraction is visible in the denser case.

To quantify this coupling further, ε_v is plotted as a function of ε_q in Fig. 6 for the increment day 0–5, plotting each point at which the strain is computed.

The displayed regression curve shows that sand dilation is clearly promoted by large ε_q for both densities (which occurs at the vicinity of the root – Fig. 4). However, the trend of ε_v differs at low ε_q between the experiments, with a slightly more contractant behaviour in the looser case (further from the root). Indeed, the density function of the volumetric strain (Fig. 6) shows that for lower intensity of ε_v, mostly contraction (positive ε_v) occurs in the looser specimen whereas dilation is predominant (negative ε_v) in the denser case.

CONCLUSIONS

Soil deformations induced by root growth has been investigated for a looser and a denser sand sample with periodic x-ray scanning, revealing significantly different soil–roots systems. A local, total, finite strain tensor is computed from displacements measured with image correlation, and the first two invariants are studied.

In both samples high values of shear strain are found around the root system, allowing a sheared sand volume to be defined where $\varepsilon_q > 1\%$ – this zone has a thickness of $\sim 10\varphi_R$ in the looser sample and $\sim 8\varphi_R$ in the denser.

In both samples, close to the root, the soil dilates. However further away from the root, volumetric deformation tends to vanish in the denser case (at a radial distance of 10–12 × D_{50}), whereas in the looser case compaction occurs at a distance 7·6–8 × D_{50}.

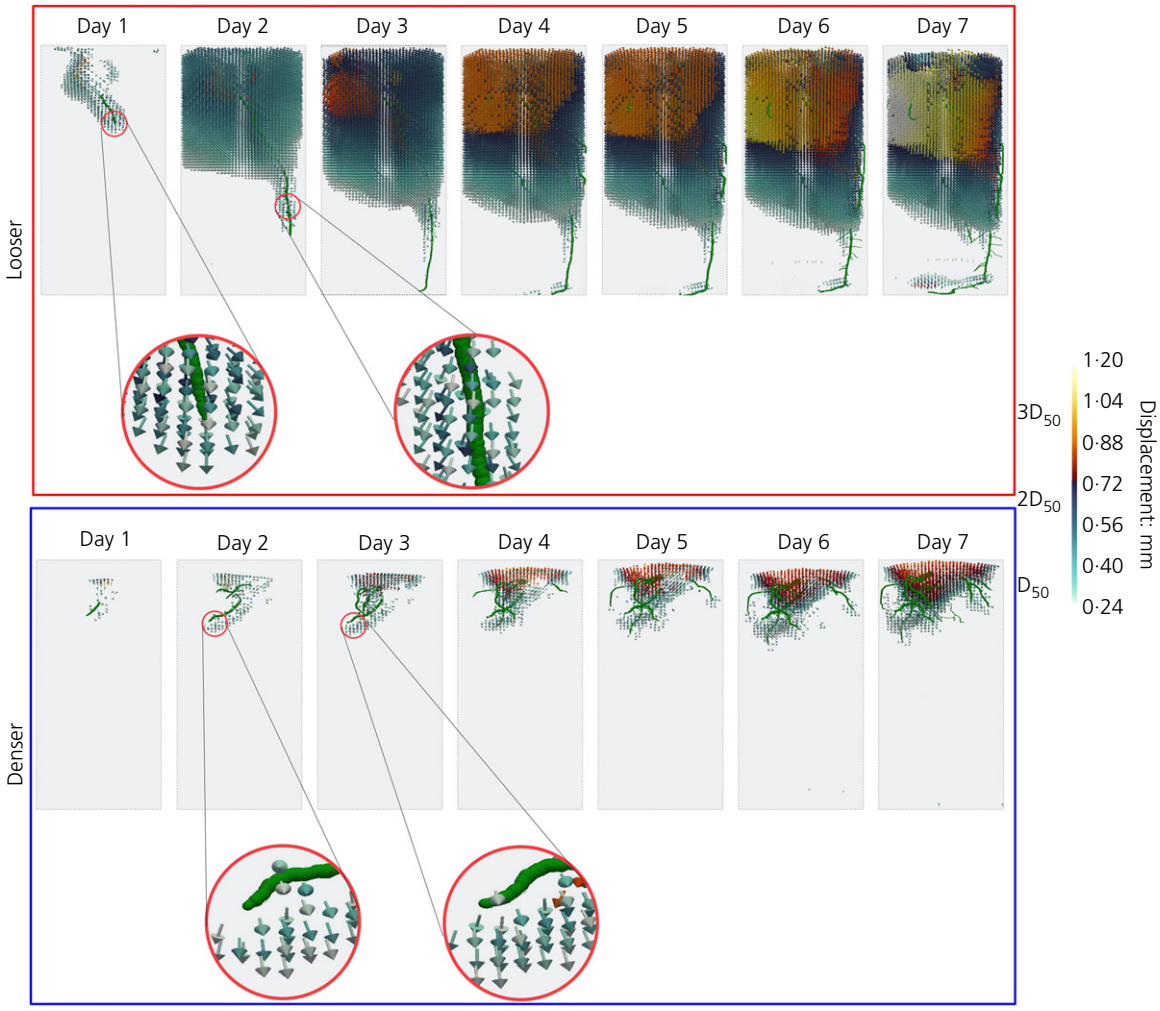

Fig. 3. 3D renderings of vector plots (quiver plot) of the displacement fields. The colour map and the arrow size indicate the magnitude of the total displacement measured in that correlation window. The root system is shown in green. For visualisation purposes, displacements smaller than ≈half D_{50} are not displayed. These renderings were made with ParaView (source: Ahrens *et al.* (2005))

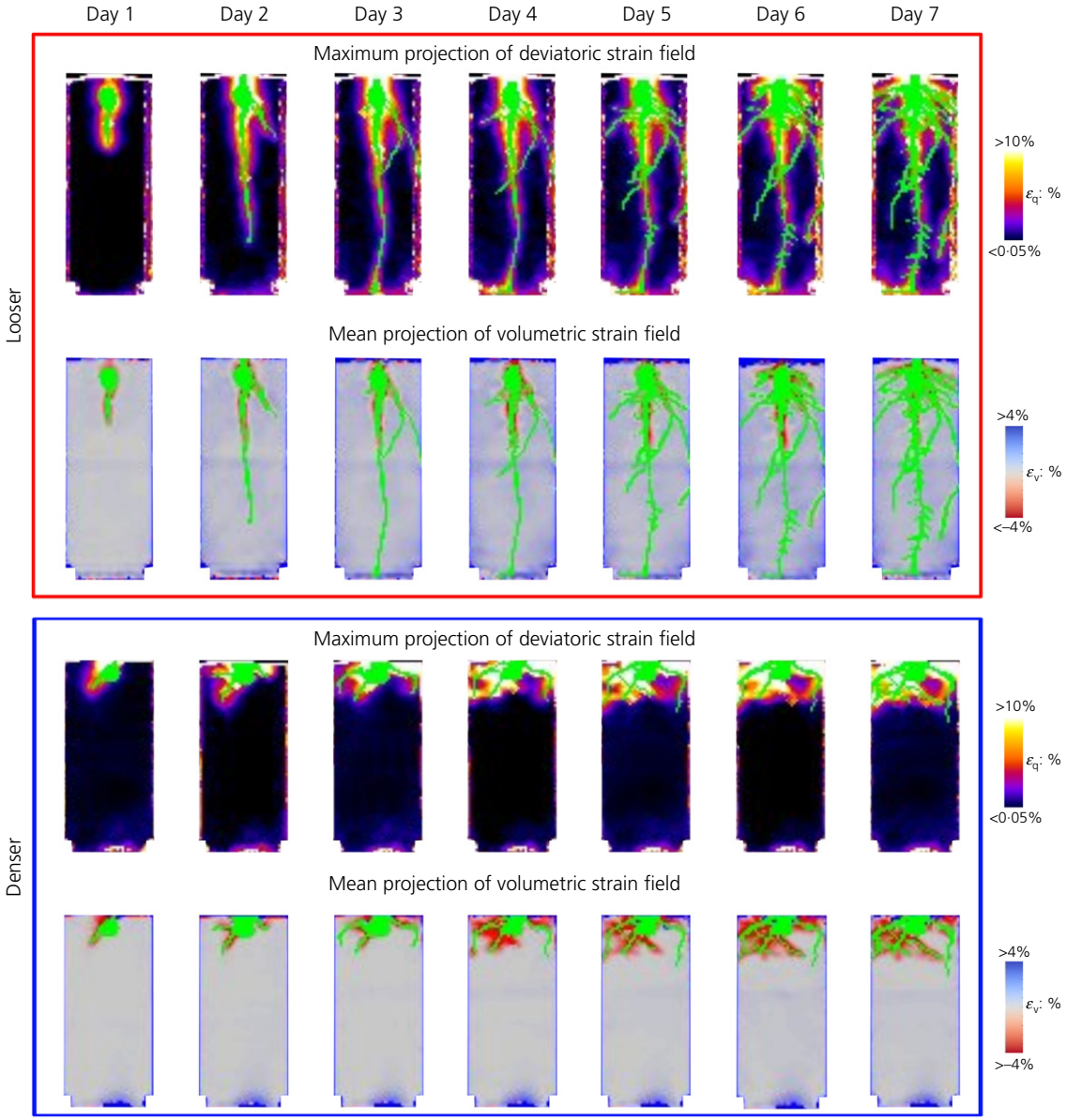

Fig. 4. Projections of the total strain fields for looser and denser sand states. In each box, top row: maximum projection of the deviatoric strain reached at that time step, bottom row: average projection of the volumetric strain reached at that time step. The projection of the root system is overlaid in green

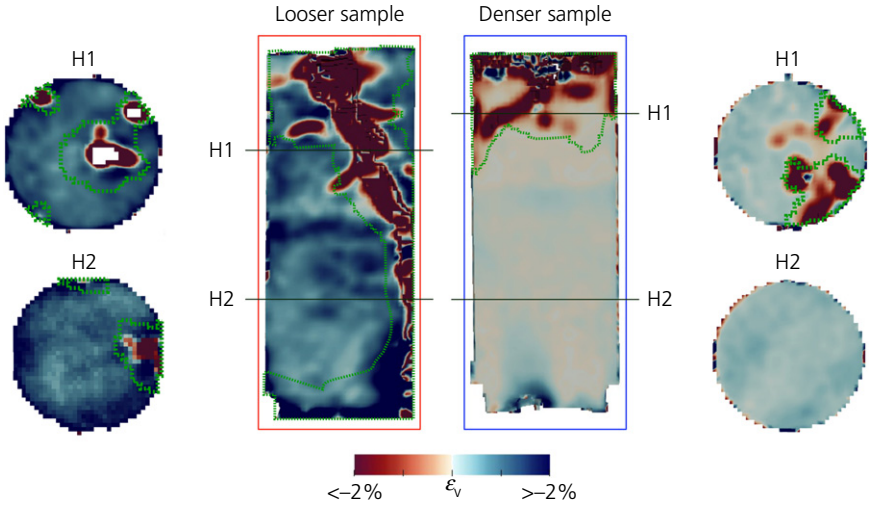

Fig. 5. Vertical and horizontal sections of the volumetric strain field; day 5. The dotted green line represents the contour of the sheared zone ($\varepsilon_q > 1\%$)

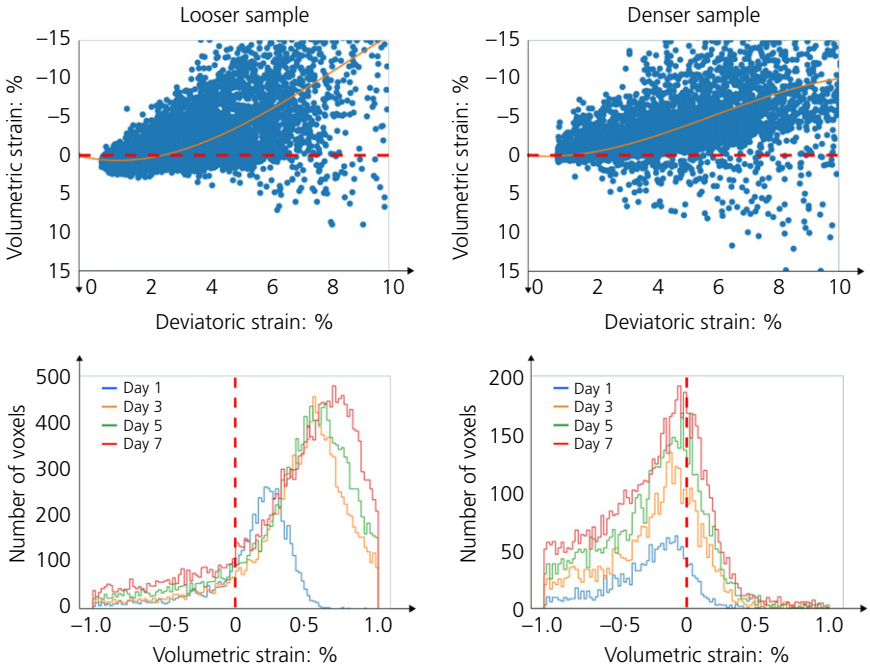

Fig. 6. First row shows the ratio between deviatoric and volumetric strain, on day 5 of the observation; second row shows the density distribution evolution of the volumetric strain trend in the portion of soil engaged with a deviatoric strain >1%

It is clear thus that the high soil porosity near the root may result not only from steric exclusion, as indicated in earlier studies, but also from the constitutive soil response to a shear deformation.

Further investigations with different bulk densities and grain-size distributions are needed to find how plant root can affect soil response. Change of water content, and thus soil suction due to the root water uptake is also an important factor that should be considered. A clear understanding of the local mechanisms involved in root–soil interactions may be taken into account in an upscaling approach and could set the base of a well-founded constitutive relation for rooted soils with application, for instance, to slope stability or soil erosion.

ACKNOWLEDGEMENTS

The authors acknowledge the French National Research Agency in the framework of the 'Investissements d'avenir' programmes referenced ANR-15-IDEX-02 (IDEX Université Grenoble Alpes) and ANR-11-LABX-0030 (LABEX Tec 21) for the financial support.

REFERENCES

Ahrens, J., Geveci, B. & Law, C. (2005). Paraview: an end-user tool for large data visualization. In *The visualization handbook*, vol. 717, No. 8. Oxford, UK: Elsevier.

Andò, E., Cailletaud, R., Roubin, E. & Stamati, O. (2017). The spam contributors, spam: The software for the practical analysis of materials.

Anselmucci, F., Andó, E., Sibille, L., Lenoir, N., Peyroux, R. & Arson, C., Viggiani, G. & Bengough, A. G. (2019). Root-reinforced sand: kinematic response of the soil. In *7th International symposium on deformation characteristics of geomaterials, IS-Glasgow 2019* (eds E. Ibraim and & A. Tarantino), vol. 92, p. 12011. Les Ulis, France: EDP Sciences.

Bengough, A., McKenzie, B., Hallett, P. & Valentine, T. (2011). Root elongation, water stress, and mechanical impedance: a review of limiting stresses and beneficial root tip traits. *J. Exp. Bot.* **62**, No. 1, 59–68.

Bodner, G., Leitner, D. & Kaul, H. (2014). Coarse and fine rooted plant species have distinct effect on soil pore size distribution. *Plant Soil* **380**, No. 1, pp. 133–151.

Canou, J. (1989). *Contribution à l'étude et à l'évaluation des propriétés de liquéfaction d'un sable.* PhD thesis, ENPC, Champs-sur-Marne, France.

Carminati, A. & Vetterlein, D. (2013). Plasticity of rhizosphere hydraulic properties as a key for efficient utilization of scarce resources. *Ann. Bot.* **112**, No. 2, 277–290.

Flavigny, E., Desrues, J. & Palayer, B. (1990). Note technique: le sable d'Hostun rf. *Rev. Française Géotech.* **53**, No. 53, 67–70.

Geers, M., De Borst, R. & Brekelmans, W. (1996). Computing strain fields from discrete displacement fields in 2D-solids. *Int. J. Solids Struct.* **33**, No. 29, 4293–4307.

Helliwell, J., Sturrock, C., Mairhofer, S., Craigon, J., Ashton, R., Miller, A., Whalley, W. & Mooney, S. (2017). The emergent rhizosphere: imaging the development of the porous architecture at the root-soil interface. *Sci. Rep.* **7**, No. 1, 1–10.

Helliwell, J., Sturrock, C., Miller, A., Whalley, W. & Mooney, S. (2019). The role of plant species and soil condition in the structural development of the rhizosphere. *Plant Cell Environ.* **42**, No. 6, 1974–1986.

Hinsinger, P., Bengough, A., Vetterlein, D. & Young, I. (2009). Rhizosphere: biophysics, biogeochemistry and ecological relevance. *Plant Soil* **321**, No. 1-2, 117–152.

Hochholdinger, F. (2009). The maize root system: morphology, anatomy, and genetics. In *Handbook of maize: its biology*, pp. 145–160. New York, NY, USA: Springer.

Jin, W., Aufrecht, J., Patino-Ramirez, F., Cabral, H., Arson, C. & Retterer, S. (2020). Modeling root system growth around obstacles. *Sci. Rep.* **10**, No. 1, 1–16.

Keyes, S., Gillard, F., Soper, N., Mavrogordato, M., Sinclair, I. & Roose, T. (2016). Mapping soil deformation around plant roots using *in vivo* 4D x-ray computed tomography and digital volume correlation. *J. Biomech.* **49**, No. 9, 1802–1811.

Keyes, S., Cooper, L., Duncan, S., Koebernick, N., McKay Fletcher, D., Scotson, C., Van Veelen, A., Sinclair, I. & Roose, T. (2017). Measurement of micro-scale soil deformation around roots using four-dimensional synchrotron tomography and image correlation. *J. R. Soc. Interface* **14**, No. 136, 20170560.

Koebernick, N., Daly, K., Keyes, S., George, T., Brown, L., Raffan, A., Cooper, L., Naveed, M., Bengough, A., Sinclair, I.

& Hallet, P. (2017). High-resolution synchrotron imaging shows that root hairs influence rhizosphere soil structure formation. *New Phytol.* **216**, No. 1, 124–135.
Lucas, M., Schlüter, S., Vogel, H. & Vetterlein, D. (2019). Roots compact the surrounding soil depending on the structures they encounter. *Sci. Rep.* **9**, No. 1, 1–13.
Lynch, J. (1995). Root Architecture and Plant Productivity. *Plant Physiol.* **109**, No. 1, 7–13.
Mallett, S., Matsumura, S. & David Frost, J. (2018). Additive manufacturing and computed tomography of bio-inspired anchorage systems. *Géotech. Lett.* **8**, No. 3, 219–225, https://doi.org/10.1680/jgele.18.00090.
Martinez, A. & Dejong, J., *et al* (2021). Bio-inspired geotechnical engineering: principles, current work, opportunities, and challenges. *Géotechnique*.
Mooney, S., Pridmore, T., Helliwell, J. & Bennett, M. (2012). Developing x-ray computed tomography to non-invasively image 3-D root systems architecture in soil. *Plant Soil* **352**, No. 1-2, 1–22.
Moreno-Espíndola, I., Rivera-Becerril, F., Jesús Ferrara-Guerrero, M. & De León-González, F. (2007). Role of root-hairs and hyphae in adhesion of sand particles. *Soil Biol. Biochem.* **39**, No. 10, 2520–2526.
Patino-Ramirez, F. & Arson, C. (2020). Transportation networks inspired by leaf venation algorithms. *Bioinspir. Biomim.* **15**, No. 3, 036012.
Stamati, O., Andò, E., Roubin, E., Cailletaud, R., Wiebicke, M., Pinzon, G., Couture, C., Hurley, R. C., Caulk, R., Caillerie, D., Matsushima, T., Bésuelle, P., Bertoni, F., Arnaud, T., Laborin, A. O., Rorato, R., Sun, Y., Tengattini, A., Okubadejo, O., Colliat, J. B., Saadatfar, M., Garcia, F. E., Papazoglou, C., Vego, I., Brisard, S., Dijkstra, J. & Birmpilis, G. (2020). Spam: software for practical analysis of materials. *J. Open Source Software* **5**, No. 51, 2286.
Świtala, B. (2020). Numerical simulations of triaxial tests on soil-root composites and extension to practical problem: rainfall-induced landslide. *Int. J. Geomech.* **20**, No. 11, 04020206.
Świtala, B., Askarinejad, A., Wu, W. & Springman, S. (2018). Experimental validation of a coupled hydro-mechanical model for vegetated soil. *Géotechnique* **68**, No. 5, 375–385, https://doi.org/10.1680/jgeot.16.P.233.
Świtala, B., Wu, W. & Wang, S. (2019). Implementation of a coupled hydro-mechanical model for root-reinforced soils in finite element code. *Comput. Geotech.* **112**, 197–203.
Tamagnini, R. (2004). An extended cam-clay model for unsaturated soils with hydraulic hysteresis. *Géotechnique* **54**, No. 3, 223–228, https://doi.org/10.1680/geot.2004.54.3.223.
Tracy, S., Black, C., Roberts, J., McNeill, A., Davidson, R., Tester, M., Samec, M., Korovsak, D., Sturrock, C. & Mooney, S. (2012). Quantifying the effect of soil compaction on three varieties of wheat (*Triticum aestivum* L.) using x-ray micro computed tomography (CT). *Plant Soil* **353**, No. 1–2, 195–208.
White, R. & Kirkegaard, J. (2010). The distribution and abundance of wheat roots in a dense, structured subsoil–implications for water uptake. *Plant Cell Environ.* **33**, No. 2, 133–148.